

Cite this: *Chem. Sci.*, 2024, 15, 4790

All publication charges for this article have been paid for by the Royal Society of Chemistry

# Realizing highly efficient deep-blue organic light-emitting diodes towards Rec.2020 chromaticity by restricting the vibration of the molecular framework†

Chuan Li,<sup>a</sup> Kai Zhang,<sup>b</sup> Yanju Luo,<sup>c</sup> Yang Yang,<sup>a</sup> Yong Huang,<sup>a</sup> Mengjiao Jia,<sup>a</sup> Yuling He,<sup>a</sup> Yue Lei,<sup>a</sup> Jian-Xin Tang,<sup>\*b</sup> Yan Huang<sup>ID</sup><sup>a</sup> and Zhiyun Lu<sup>ID</sup><sup>\*a</sup>

Deep-blue organic light-emitting diodes (OLEDs) with narrow emission spectra and high efficiency, meeting the Rec.2020 standard, hold significant promise in the realm of 4K/8K ultrahigh-definition displays. However, the development of light-emitting materials exhibiting both narrowband emission and high efficiency, particularly in the realm of deep-blue thermally activated delayed fluorescence (TADF), confronts substantial challenges. Herein, a novel deep-blue TADF emitter, named BOC-PSi, was designed by integrating a rigid B-heterotriangulene acceptor (A) with a rigid phenazasiline donor (D). The replacement of a sp<sup>3</sup> carbon atom with a sp<sup>3</sup> silicon atom in the D moiety helps to restrict the low-frequency bending vibration throughout the entire D–A molecular backbone, while concurrently accelerating the multi-channel reverse intersystem crossing (RISC) processes. Notably, OLEDs using the BOC-PSi emitter exhibit exceptional performance, with a high maximum external quantum efficiency (EQE<sub>max</sub>) approaching 20%, and a superior color purity closely aligning with the Rec.2020 blue standard.

Received 16th December 2023  
Accepted 20th February 2024

DOI: 10.1039/d3sc06763g

rs.c.li/chemical-science

## Introduction

Narrow-emission and highly efficient blue thermally activated delayed fluorescence (TADF) materials approaching the Rec.2020 standard for color gamut (CIE coordinates: (0.131, 0.046), as recommended by the International Telecommunication Union) have attracted significant research attention due to their immense potential in the field of 4K/8K ultrahigh-definition displays.<sup>1,2</sup> However, the development of such materials has encountered considerable challenges, as it requires concurrent optimization of the high photoluminescence (PL) efficiency ( $\Phi_{\text{PL}}$ ), narrow full width at half maximum (FWHM), fast reverse intersystem crossing (RISC) process, and wide bandgap. Therefore, only a handful of reports exist on blue TADF organic light-emitting diodes (OLEDs) with a CIE<sub>y</sub> value

close to 0.046 and a maximum external quantum efficiency (EQE<sub>max</sub>) surpassing 15%.<sup>3–7</sup>

To achieve TADF materials with a narrow emission bandwidth, it is essential to impart a rigid framework to the fluorophore. A notable example of this concept is multiple resonance (MR) B,N-heteroarenes, known for exhibiting narrow FWHM and high  $\Phi_{\text{PL}}$  due to their highly rigid molecular scaffolds.<sup>8–10</sup> Nevertheless, their robust planar molecular backbones significantly hinder the realization of strong spin-orbit coupling (SOC).<sup>11</sup> As a result, most MR-TADF dyes experience relatively slow RISC processes, posing challenges for their implementation in conventional TADF-OLEDs without the need supplementary TADF sensitizers.

On the other hand, due to the compensating effect between their variations in orbital angular momentum and spin angular momentum,<sup>12,13</sup> TADF molecules with highly distorted donor–acceptor (D–A) structures are more likely to exhibit a relatively fast RISC process. However, as the D and A moieties are chemically linked only through a fragile single bond, these D–A dyads generally suffer from poor framework rigidity, leading to a relatively wide FWHM and an accelerated non-radiative process. Moreover, to minimize the singlet–triplet energy gap ( $\Delta E_{\text{ST}}$ ), these D–A TADF compounds often possess a nearly orthogonal orientation between their D and A units, resulting in a reduced radiative transition rate. Consequently, the accelerated non-radiative process poses a significant obstacle to achieving a high  $\Phi_{\text{PL}}$ .

<sup>a</sup>Key Laboratory of Green Chemistry and Technology (Ministry of Education), College of Chemistry, Sichuan University, Chengdu 610064, P. R. China. E-mail: luzhiyun@scu.edu.cn

<sup>b</sup>Macau Institute of Materials Science and Engineering (MIMSE), Faculty of Innovation Engineering, Macau University of Science and Technology, Taipa, Macau SAR 999078, P. R. China. E-mail: jxtang@must.edu.mo

<sup>c</sup>Analytical & Testing Center, Sichuan University, Chengdu 610064, P. R. China

† Electronic supplementary information (ESI) available: Experimental procedures, computational details, <sup>1</sup>H and <sup>13</sup>C NMR spectra, HRMS, and single-crystal XRD structures of the target compounds. CCDC 2307420–2307421. For ESI and crystallographic data in CIF or other electronic format see DOI: <https://doi.org/10.1039/d3sc06763g>



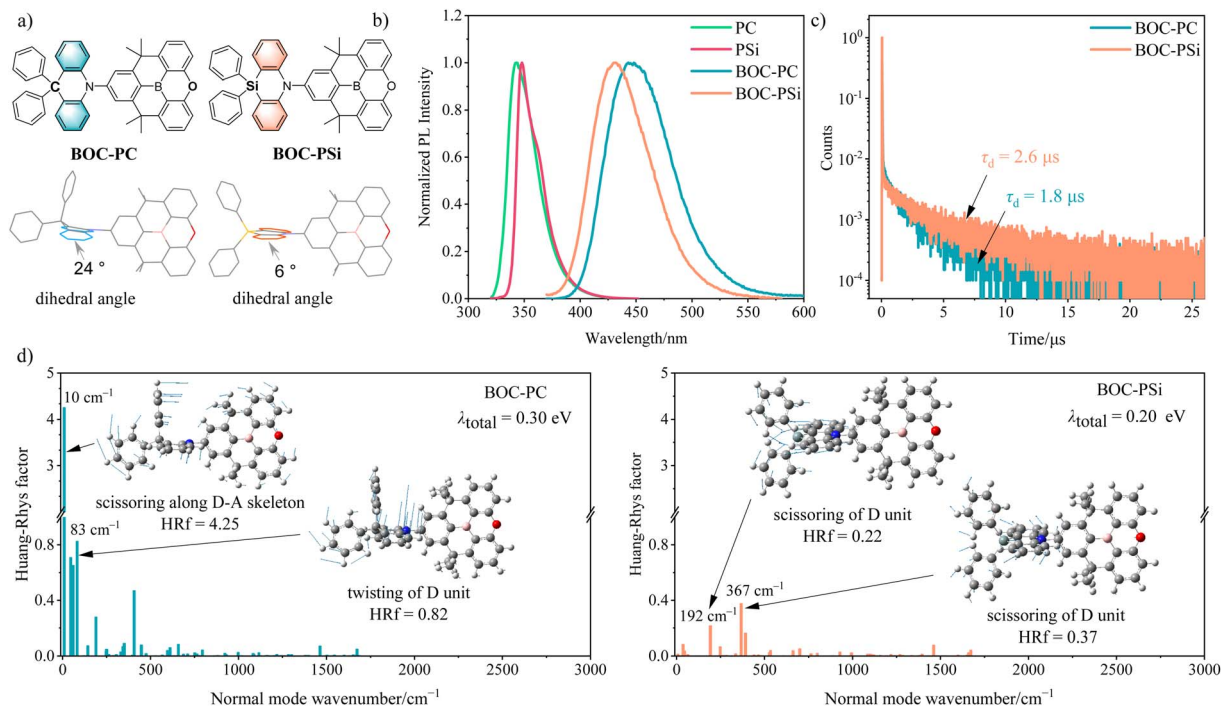


Fig. 1 (a) Molecular and single crystal structures of BOC-PC and BOC-PSi; (b) PL spectra of PC, PSi, BOC-PC and BOC-PSi (in toluene at a concentration of 10  $\mu\text{M}$ ); (c) PL decay curves of BOC-PC- and BOC-PSi-based film samples (15 wt% in DPEPO under  $\text{N}_2$ ); (d) calculated Huang-Rhys factors and corresponding vibration modes contributed significantly to the reorganization energy of BOC-PC and BOC-PSi from the  $\text{S}_1$  to  $\text{S}_0$  states (PBE0/6-31G\*\* at optimized  $\text{S}_1$  geometry).

In addition, to obtain TADF D-A dyads with deep-blue emission performance approaching the Rec.2020 standard, it is necessary to carefully select D and A moieties not only having a deep highest occupied molecular orbital (HOMO) and a shallow lowest unoccupied molecular orbital (LUMO), respectively, but also possessing a local triplet excited state ( $^3\text{LE}$ ) energy level higher than 3.0 eV. However, such structural units are scarce, which further adds to the challenge of constructing TADF emitters with a wide bandgap.<sup>14</sup>

Herein, we report a high-performance deep-blue TADF D-A dyad, namely **BOC-PSi**, which utilizes a rigid B-heterotriangulene derivative (BOC) as the A moiety, and 10,10-diphenyl-5,10-dihydrodibenzo[*b,e*][1,4]azasiline (PSi), the sila-product of 9,9-diphenyl-9,10-dihydroacridine (PC), as the D moiety (Fig. 1a). **BOC-PSi**-based OLEDs demonstrated an  $\text{EQE}_{\text{max}}$  of 19.6% under a  $\text{CIE}_y$  value of 0.049, establishing **BOC-PSi** as an advanced Rec.2020 blue OLED emitter (Table S3<sup>†</sup>). Comparative studies between **BOC-PSi** and **BOC-PC** (a reference compound using PC as the D unit) revealed that the better electroluminescence (EL) performance of **BOC-PSi** can be mainly attributed to its narrower FWHM and higher  $\Phi_{\text{PL}}$ , which arise from the enhanced rigidity of PSi compared to PC. These findings demonstrated that D-A TADF dyads with exceptional blue color gamut can be acquired by employing rigid D and A subunits.

## Molecular design rationale & characterization

The design rationale for **BOC-PSi** is as follows. (1) To endow the dyad with a highly twisted geometry, PC composed of merely

six-membered polycyclic ring systems was chosen as the parent D scaffold.<sup>15</sup> (2) A sila-modification was performed on PC, because the resulting PSi shows better framework rigidity compared to PC, as evidenced by its narrower and more structured fluorescence and phosphorescence spectra (Fig. 1b and S8<sup>†</sup>). (3) The  $^3\text{LE}$  energy level of PSi is as high as 3.10 eV, and its calculated HOMO (−5.60 eV) is deeper than that of PC, which may be attributed to the weaker hyperconjugation effects in PSi (Fig. S11<sup>†</sup>).<sup>16,17</sup> These conditions facilitate the acquisition of a TADF D-A dyad with a wide bandgap. (4) Based on the HOMO energy level data of PSi, BOC was screened out as the A moiety due to its integrated rigid molecular skeleton, high  $^3\text{LE}$  energy level of 3.17 eV, and shallow LUMO level of −2.36 eV.<sup>18</sup>

The synthetic routes of **BOC-PSi** and **BOC-PC** are illustrated in the ESI (Scheme S1).<sup>†</sup> The molecular structure of **BOC-PSi** and **BOC-PC** was confirmed by nuclear magnetic resonance spectroscopy (NMR), high-resolution mass spectroscopy (MS), and single crystal X-ray diffraction (XRD).

The single crystal structures of **BOC-PSi** and **BOC-PC** are depicted in Fig. S10,<sup>†</sup> and the corresponding crystal parameters are listed in Table S1.<sup>†</sup> As expected, **BOC-PSi** and **BOC-PC** both show a nearly perpendicular orientation between their D and A segments, with torsion angles measuring 86.4° and 84.0°, respectively. This highly twisted geometry offers advantages in promoting efficient RISC by facilitating enhanced vibronic coupling between the charge-transfer triplet excited state ( $^3\text{CT}$ ) and  $^3\text{LE}$  state. However, the two phenyl substituents of D units in the two compounds have quite different relative positions. As shown in Fig. 1a, the two phenyls of **BOC-PSi** are nearly



symmetrically distributed above and below the azasiline plane, whereas those of **BOC-PC** exhibit distinct conformations, with one quasi-axial and the other quasi-equatorial. The disparity in the relative positions of the phenyls of **BOC-PSi** and **BOC-PC** can be attributed to the more planar configuration of the azasiline ring compared to the acridine ring (dihedral angle:  $\sim 6^\circ$  vs.  $\sim 24^\circ$ , Fig. 1a and S10<sup>†</sup>), which is due to the significantly longer  $C_{sp^2}-Si_{sp^3}$  bonds than the corresponding  $C_{sp^2}-C_{sp^3}$  bonds ( $\sim 1.8$  vs.  $\sim 1.5$  Å, Table S1<sup>†</sup>), resulting from the larger atomic radius of silicon than carbon.

## Electrochemical & thermal stability properties

Through cyclic voltammetry (CV) measurements (Fig. S5<sup>†</sup>), the HOMO energy level values of **BOC-PC** and **BOC-PSi** were determined to be  $-5.41$  eV and  $-5.53$  eV, respectively. The deeper HOMO level of **BOC-PSi** than **BOC-PC** indicates the weaker electron-donating ability of PSi compared to PC, which ultimately benefits the realization of wider bandgap emission. Subsequently, the LUMO energy level values were calculated from the corresponding optical bandgap and HOMO energy level data, and were determined to be  $-2.32$  eV and  $-2.37$  eV for **BOC-PC** and **BOC-PSi**, respectively. The slight disparity in the LUMO energy level values between the two compounds could potentially stem from the variation in the D–A dihedral angles in their optimized  $S_0$  geometrical structures (Fig. S12<sup>†</sup>).

Based on the results of thermal gravimetry analysis (TGA) and differential scanning calorimetry (DSC) characterizations (Fig. S6<sup>†</sup>), both compounds demonstrate excellent thermal stability, as evidenced by their high decomposition temperatures ( $T_d$ ) exceeding  $340$  °C at 5% initial weight loss. In addition, only **BOC-PC** exhibits a notably high melt temperature ( $T_m$ ) of  $327$  °C, while no significant endothermic signal ascribed to glass transition could be observed in both emitters.

## Photoluminescence properties

The photophysical properties of these two emitters were investigated in dilute solution ( $10^{-5}$  M) and doped film states (15 wt% in bis[2-(diphenylphosphino)phenyl]ether oxide (DPEPO)). As illustrated in Fig. 1b and Table 1, **BOC-PSi** and **BOC-PC** both emit deep-blue PL in toluene, but **BOC-PSi** exhibits a superior blue color gamut to **BOC-PC** due to its  $>10$  nm blue-shifted PL emission band ( $\lambda_{PL}$ :  $432$  vs.  $445$  nm) and much narrowed FWHM ( $61$  vs.  $70$  nm). These findings provide clear evidence for the effectiveness of this strategy in the rational design of deep-blue emitters. Besides, with increasing

solvent polarity from hexane to acetonitrile, both **BOC-PSi** and **BOC-PC** display red-shifted and broadened PL spectra, manifesting the CT character of their  $S_1$  states (Fig. S7<sup>†</sup>). Notably, **BOC-PSi** consistently shows a narrower PL spectrum compared to **BOC-PC** in every solvent, suggesting that a more rigid D subunit can indeed induce a narrower FWHM of the corresponding  $^1CT$ -featured emission in a D–A dyad.

In terms of the two film samples, they both exhibit slightly narrowed PL spectra compared to their corresponding toluene solutions (FWHM:  $55$  vs.  $61$  nm for **BOC-PSi**;  $66$  vs.  $70$  nm for **BOC-PC**), which can be attributed to the restricted rotation of the C–N single bond within a more rigid matrix. In comparison to **BOC-PC**, **BOC-PSi** also shows a blue-shifted ( $\lambda_{PL}$ :  $439$  vs.  $454$  nm) PL spectrum with a narrowed FWHM ( $55$  vs.  $66$  nm). Additionally, **BOC-PSi** shows a higher  $\Phi_{PL}$  compared to **BOC-PC** ( $92\%$  vs.  $80\%$ ), indicative of the existence of additional exciton loss pathways in **BOC-PC**, potentially arising from the vibration relaxation of the fluorophore.

Further transient PL measurements revealed the presence of delayed fluorescence (DF) behavior in both film samples. Notably, the DF lifetime ( $\tau_{DF}$ ) is as short as  $2.6$   $\mu$ s for **BOC-PSi** and  $1.8$   $\mu$ s for **BOC-PC** (Fig. 1c), indicative of the occurrence of fast RISC processes in both **BOC-PSi** and **BOC-PC**. With respect to the prompt fluorescence (PF), the average lifetime ( $\tau_{PF}$ ) is determined to be  $9.4$  ns for **BOC-PSi** and  $14.2$  ns for **BOC-PC** (Fig. S9<sup>†</sup>). Based on the  $\tau_{DF}$ ,  $\tau_{PF}$ ,  $\Phi_{PF}$  and  $\Phi_{DF}$  data (Table 1), the rate constants for key photophysical processes, including fluorescence decay ( $k_F$ ), intersystem crossing ( $k_{ISC}$ ), RISC ( $k_{RISC}$ ), and non-radiative decay of the  $S_1$  state ( $k_{NR}^S$ ), were calculated for the two compounds.<sup>19,20</sup>

## Exciton dynamics process

As shown in Table 1, **BOC-PSi** has a significantly smaller  $k_{NR}^S$  than **BOC-PC** ( $2.41 \times 10^6$  vs.  $8.63 \times 10^6$   $s^{-1}$ ). To elucidate the underlying cause of the suppressed non-radiative process resulting from the sila-modification, theoretical calculations were conducted to determine the total reorganization energy ( $\lambda_{total}$ ) between the  $S_1$  and  $S_0$  states for both compounds as well as the A moiety of BOC. The results indicated that the  $\lambda_{total}$  of **BOC-PSi** is slightly smaller than that of **BOC-PC** ( $0.20$  vs.  $0.30$  eV, vide Fig. 1d), implying that **BOC-PSi** possesses superior molecular skeleton rigidity to **BOC-PC**,<sup>21,22</sup> while the  $\lambda_{total}$  of BOC is only  $0.17$  eV, indicative of its excellent rigidity (Fig. S14<sup>†</sup>). In line with this deduction, the root mean square deviation (RMSD) value of the superposition of the optimized  $S_0$  and  $S_1$  geometries of **BOC-PSi** is much smaller than that of **BOC-PC** ( $0.123$  vs.  $0.316$  Å, Fig. S15<sup>†</sup>).<sup>24</sup> These findings suggest a stronger suppression of non-radiative decay for the  $S_1$  state of **BOC-PSi** than **BOC-PC**.

Table 1 Key photophysical data of **BOC-PC** and **BOC-PSi** (15 wt%-doped in DPEPO under  $N_2$ )

| Compound       | $\lambda_{PL}$ [nm] | $\Phi_{PL}$ | $\Phi_{PF}$ | $\Phi_{DF}$ | $\Phi_{ISC}$ | $\tau_{PF}$ [ns] | $\tau_{DF}$ [ $\mu$ s] | $k_F$ [ $s^{-1}$ ] | $k_{ISC}$ [ $s^{-1}$ ] | $k_{RISC}$ [ $s^{-1}$ ] | $k_{NR}^S$ [ $s^{-1}$ ] |
|----------------|---------------------|-------------|-------------|-------------|--------------|------------------|------------------------|--------------------|------------------------|-------------------------|-------------------------|
| <b>BOC-PC</b>  | 454                 | 80%         | 49%         | 31%         | 39%          | 14.2             | 1.8                    | $3.45 \times 10^7$ | $2.73 \times 10^7$     | $9.07 \times 10^5$      | $8.63 \times 10^6$      |
| <b>BOC-PSi</b> | 439                 | 92%         | 26%         | 66%         | 72%          | 9.4              | 2.6                    | $2.77 \times 10^7$ | $7.63 \times 10^7$     | $1.36 \times 10^6$      | $2.41 \times 10^6$      |





To elucidate the reason for the disparity in FWHM between the two emitters, the Huang–Rys factors (HRf) at various vibration modes were calculated for **BOC-PSi**, **BOC-PC** and **BOC**. For **BOC-PC**, a low-frequency scissoring swing of the entire molecular framework was observed at a normal mode wavenumber of  $10\text{ cm}^{-1}$  (Fig. 1d and S13†), accompanied by a large HRf of 4.25.<sup>23</sup> Detailed vibration mode analysis revealed that the scissoring motion along the D–A skeleton in **BOC-PC** can be ascribed to the top-heavy nature of its PC moiety during the bending vibration of the C–N bond. Additionally, the vibration mode in **BOC-PC** that exhibits the second-largest HRf (0.82) also arises from the twisting of the PC moiety. In contrast, due to the well-balanced character of its PSi moiety, all HRfs calculated at the low-frequency region below  $200\text{ cm}^{-1}$  are significantly smaller than those of **BOC-PC**, and no obvious vibrational motions throughout the whole D–A scaffold of **BOC-PSi** were observed. Therefore, the **BOC-PSi** exhibits a smaller overall HRf compared to **BOC-PC**, manifesting a significantly suppressed structural relaxation thus narrowing the FWHM.<sup>24</sup> In the case of **BOC**, no detectable vibrations were found contributing to its HRf in the low-frequency range below  $200\text{ cm}^{-1}$ , indicative of its excellent skeletal rigidity. Therefore, it can be inferred that the severe non-radiative process and larger FWHM in **BOC-PC** should be mainly ascribed to its PC subunit.

Excitingly, the  $k_{\text{ISC}}$  and  $k_{\text{RISC}}$  values of **BOC-PSi** are also both larger than those of **BOC-PC** ( $k_{\text{ISC}}$ :  $7.63 \times 10^7$  vs.  $2.73 \times 10^7\text{ s}^{-1}$ ;  $k_{\text{RISC}}$ :  $1.36 \times 10^6$  vs.  $9.07 \times 10^5\text{ s}^{-1}$ ), indicating a stronger SOC effect and/or a smaller energy difference between the  $S_1$  and  $T_1/T_n$  states in **BOC-PSi**. To understand the reason behind the larger  $k_{\text{RISC}}$  value of **BOC-PSi** than **BOC-PC**, the PL and phosphorescence (Phos) spectra of both compounds were recorded at 77 K. The structureless and red-shifted PL and Phos spectra of the two compounds relative to their corresponding D/A fragments manifest the  $^1\text{CT}$  and  $^3\text{CT}$  features of their  $S_1$  and  $T_1$  states, respectively (Fig. S8†). The  $^1\text{CT}/^3\text{CT}$  energy levels, according to the onset of the PL and Phos spectra, were estimated to be 3.06/2.99 eV for **BOC-PC** and 3.11/3.05 eV for **BOC-PSi**. Although the singlet-triplet splitting of the CT excited states in **BOC-PC** and **BOC-PSi** is quite similar (0.07 vs. 0.06 eV), there is an evident difference in the energy splitting between their  $^1\text{CT}$  and  $^3\text{LE}_D/^3\text{LE}_A$  states. As depicted in Fig. S8,† the  $^3\text{LE}$  energy levels of PC and PSi were both calculated to be approximately 3.20 eV, while that of **BOC** was estimated to be 3.35 eV. Therefore, the absolute values of  $\Delta E_{\text{ST}}(^1\text{CT}-^3\text{LE}_D)$  and  $\Delta E_{\text{ST}}(^1\text{CT}-^3\text{LE}_A)$  of **BOC-PC** are 0.14 eV and 0.29 eV, respectively, whereas those for **BOC-PSi** are 0.09 eV and 0.24 eV respectively. Considering that D–A dyads with highly twisted molecular geometries typically exhibit a much stronger SOC effect between a  $^3\text{LE}$  and a  $^1\text{CT}$  state compared to that between a  $^3\text{CT}$  and a  $^1\text{CT}$

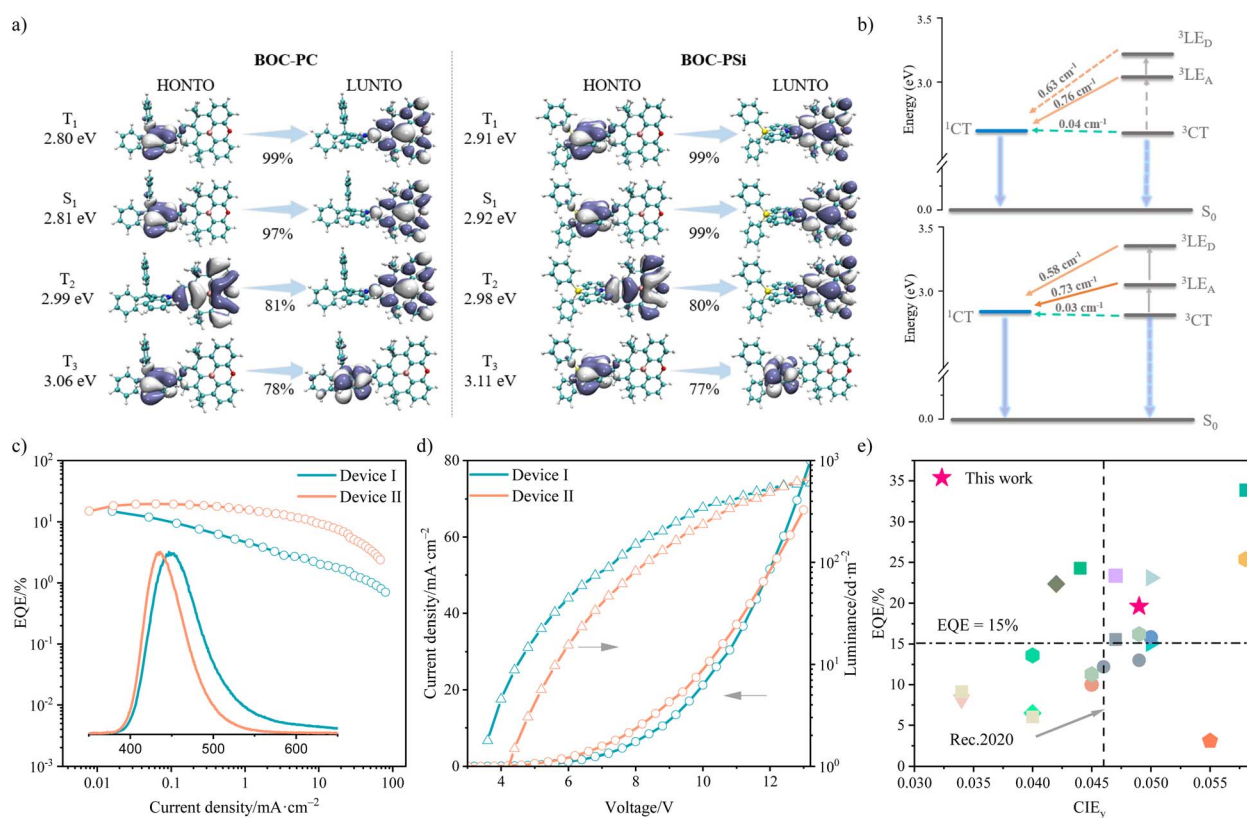


Fig. 2 (a) Calculated excited states energy and NTO distributions for **BOC-PC** and **BOC-PSi**; (b) the plausible mechanism of harvesting triplet states for **BOC-PC** (top) and **BOC-PSi** (bottom); (c) EQE as a function of the current density ( $J$ ) of **BOC-PC**-based device I, and **BOC-PSi**-based device II (inset: EL spectra of devices I–II at  $J$  of  $10\text{ mA cm}^{-2}$ ); (d) current density–voltage–luminance ( $J$ – $V$ – $L$ ) profiles of devices I–II; (e) comparison of EQE<sub>max</sub> for the reported deep-blue OLED with CIE<sub>y</sub> of 0.03–0.06.



Table 2 The key EL properties of BOC-PSi- and BOC-PC-based OLEDs

| Dopant         | Device | $\lambda_{\text{EL}}$ (nm) | FWHM (nm) | CE <sub>max</sub> (cd A <sup>-1</sup> ) | EQE <sup>a</sup> /EQE <sup>b</sup> (%) | Roll-off <sup>c</sup> | CIE <sub>1931</sub> (x, y) |
|----------------|--------|----------------------------|-----------|---|--|-----------------------|----------------------------|
| <b>BOC-PC</b>  | I      | 450                        | 62        | 11.12                                   | 14.8/2.8                               | 85%                   | (0.148, 0.085)             |
| <b>BOC-PSi</b> | II     | 433                        | 53        | 9.10                                    | 19.6/14.8                              | 24%                   | (0.154, 0.049)             |

<sup>a</sup> Device maximum external quantum efficiency. <sup>b</sup> External quantum efficiency at 100 cd m<sup>-2</sup>. <sup>c</sup> Efficiency roll off from 1 cd m<sup>-2</sup> to 100 cd m<sup>-2</sup>.

state,<sup>13</sup> the faster RISC process in **BOC-PSi**, as compared to **BOC-PC**, may be attributed to the smaller absolute values of  $\Delta E_{\text{ST}}$  (<sup>1</sup>CT-<sup>3</sup>LE).

This deduction was supported by theoretical computations. As depicted in Fig. 2a, the S<sub>1</sub> and T<sub>1</sub> states of **BOC-PC** and **BOC-PSi** were both calculated to show a CT feature, and the energy splitting between the two states is 0.01 eV for both compounds. In line with our conjecture, the calculated SOC constants for the T<sub>1</sub> → S<sub>1</sub> process are 0.04 cm<sup>-1</sup> for **BOC-PC** and 0.03 cm<sup>-1</sup> for **BOC-PSi**, both are too small to trigger fast RISC processes. Nevertheless, the T<sub>2</sub> states of **BOC-PC** and **BOC-PSi** are both dominated by the BOC unit, displaying a <sup>3</sup>LE<sub>A</sub> character. Despite having an identical T<sub>2</sub> energy level (~3.0 eV), the lower S<sub>1</sub> state of **BOC-PC** results in a larger absolute value of  $\Delta E_{\text{ST}}$  (<sup>1</sup>CT-<sup>3</sup>LE<sub>A</sub>) compared to **BOC-PSi** (0.18 vs. 0.06 eV). Considering that the SOC constants between the T<sub>2</sub> and S<sub>1</sub> states of **BOC-PC** and **BOC-PSi** are relatively large (>0.70 cm<sup>-1</sup>), both compounds are expected to undergo a relatively fast T<sub>2</sub> → S<sub>1</sub> RISC process. However, **BOC-PSi** is likely to achieve a larger *k*<sub>RISC</sub> due to its much smaller  $\Delta E_{\text{ST}}$  (<sup>1</sup>CT-<sup>3</sup>LE<sub>A</sub>) value compared to **BOC-PC**. Additionally, for **BOC-PSi**, its T<sub>3</sub> state (exhibiting a <sup>3</sup>LE<sub>D</sub> character) was found to be close to its S<sub>1</sub> state ( $\Delta E_{\text{ST}} = 0.20$  eV), and the calculated SOC constant for the T<sub>3</sub> → S<sub>1</sub> process was also substantial at 0.58 cm<sup>-1</sup>, implying the presence of a fast T<sub>3</sub> → S<sub>1</sub> RISC process in **BOC-PSi**. Consequently, the large *k*<sub>RISC</sub> of **BOC-PSi** is believed to stem from its effective multi-channel RISC processes.

Therefore, through the substitution of the sp<sup>3</sup>-C atom within the 9,10-diphenylacridine segment of **BOC-PC** with a sp<sup>3</sup>-Si, we have acquired **BOC-PSi**, which has a better-balanced and robust molecular framework, a slightly deepened HOMO energy level, and a maintained high <sup>3</sup>LE energy level. As a result, in comparison to **BOC-PC**, **BOC-PSi** shows a wider emission bandgap, a narrower FWHM, a more suppressed non-radiative process and hence a higher  $\Phi_{\text{PL}}$ , as well as a faster RISC process. Consequently, it is expected that **BOC-PSi** will demonstrate superior EL performance to **BOC-PC**.

## Electroluminescence performance

Subsequently, OLEDs were fabricated using **BOC-PSi** or **BOC-PC** as the doping guest (15 wt% in DPEPO): ITO/PEDOT: PSS (30 nm)/TAPC (30 nm)/TCTA (10 nm)/mCP (10 nm)/DPEPO: emitters (15 wt%, 40 nm)/DPEPO (5 nm)/TmPyPB (35 nm)/LiF (1.2 nm)/Al (120 nm). Consistent with our conjecture, the **BOC-PSi**-based device II shows significantly superior EL performance to the **BOC-PC**-based device I. As depicted in Table 2, device I

displayed an inferior EL color purity than device II (CIE<sub>y</sub>: 0.085 vs. 0.049) due to the red-shifted EL band ( $\lambda_{\text{EL}}$ : 450 vs. 433 nm) and wide FWHM (62 vs. 52 nm). Besides, device I also exhibited a lower EQE<sub>max</sub> (14.8% vs. 19.6%) together with more pronounced efficiency roll-off. These disadvantages can be ascribed to the narrower emission bandgap, wider FWHM, lower  $\Phi_{\text{PL}}$  and slower RISC process of **BOC-PC** than **BOC-PSi**. All these findings confirm the potential of **BOC-PSi** as a more promising deep-blue OLED emitter than **BOC-PC**. It is noteworthy that the **BOC-PSi**-based OLEDs stand as one of the top-performing examples among reported deep blue TADF OLEDs whose color purity approaches the Rec.2020 blue standard.

## Conclusion

In conclusion, we demonstrated that by employing rigid D and A structural units, TADF D-A dyads with narrow FWHM and high  $\Phi_{\text{PL}}$  can be developed. Using **BOC-PSi** as an example, we proved that 10,10-diphenyl-5,10-dihydrodibenzo[*b,e*][1,4]azasiline (PSi) is a more promising D unit than 9,9-diphenyl-9,10-dihydroacridine (PC) when constructing deep blue TADF D-A dyads with good color gamut. The reason for this is that the replacement of a sp<sup>3</sup>-C with a sp<sup>3</sup>-Si helps to restrict the low-frequency bending vibration along the whole D-A molecular backbone, thus minimizing exciton energy loss, while concurrently accelerating the multi-channel RISC processes. OLEDs using **BOC-PSi** as the emitter exhibited not only an impressive EQE<sub>max</sub> of nearly 20% and a narrow FWHM of 53 nm, but also a superior color purity approaching the Rec.2020 blue standard. This work would provide a new avenue in developing highly efficient, narrow-emission and wide-bandgap blue TADF-OLED materials.

## Data availability

Experimental procedures, details of the calculations, and additional data can be found in the ESI.†

## Author contributions

C. L., K. Z. and Y. L. contributed equally to this work. C. L. – conceptualization, synthesis, investigation, visualization, writing – original draft; K. Z. – OLED devices, investigation; Y. L. – investigation, funding acquisition, writing – review & editing; Y. Y. – investigation (photophysics); Y. H. – investigation (photophysics); M. J. – investigation (photophysics); Y. H. – investigation (photophysics); Y. L. – synthesis; J. T. – funding



acquisition, OLED devices, review & editing; Y. H. – review & editing; Z. L. – funding acquisition, project administration, writing – review & editing, conceptualization, supervision.

## Conflicts of interest

There are no conflicts to declare.

## Acknowledgements

The authors gratefully acknowledge the financial support from the National Natural Science Foundation of China (no. 22105136 and 22075187), the Science and Technology Development Fund (FDCT), Macau SAR (no. 0008/2022/AMJ), the China Postdoctoral Science Foundation (no. 2021M702324) and Fundamental Research Funds for the Central Universities. The authors thank Dr Peng Wu and Dr Yang Feng of the Analytical & Testing Center and Dr Meng Yang of the College of Chemistry, Sichuan University for photophysical and molecular structure characterizations.

## References

- 1 J. M. Ha, S. H. Hur, A. Pathak, J.-E. Jeong and H. Y. Woo, Recent advances in organic luminescent materials with narrowband emission, *NPG Asia Mater.*, 2021, **13**, 53.
- 2 R. K. Konidena and K. R. Naveen, Boron-Based Narrowband Multiresonance Delayed Fluorescent Emitters for Organic Light-Emitting Diodes, *Adv. Photonics Res.*, 2022, **3**, 2200201.
- 3 H. J. Kim, H. Kang, J. E. Jeong, S. H. Park, C. W. Koh, C. W. Kim, H. Y. Woo, M. J. Cho, S. Park and D. H. Choi, Ultra-Deep-Blue Aggregation-Induced Delayed Fluorescence Emitters: Achieving Nearly 16% EQE in Solution-Processed Nondoped and Doped OLEDs with CIEy < 0.1, *Adv. Funct. Mater.*, 2021, **31**, 2102588.
- 4 V. V. Patil, H. L. Lee, I. Kim, K. H. Lee, W. J. Chung, J. Kim, S. Park, H. Choi, W. J. Son, S. O. Jeon and J. Y. Lee, Purely Spin-Vibronic Coupling Assisted Triplet to Singlet Up-Conversion for Real Deep Blue Organic Light-Emitting Diodes with Over 20% Efficiency and  $\gamma$  Color Coordinate of 0.05, *Adv. Sci.*, 2021, **8**, 2101137.
- 5 H.-J. Tan, G.-X. Yang, Y.-L. Deng, C. Cao, J.-H. Tan, Z.-L. Zhu, W.-C. Chen, Y. Xiong, J. X. Jian, C.-S. Lee and Q.-X. Tong, Deep-Blue OLEDs with Rec.2020 Blue Gamut Compliance and EQE over 22% Achieved by Conformation Engineering, *Adv. Mater.*, 2022, **34**, 2200537.
- 6 J. Kang, S. O. Jeon, H. L. Lee, J. Lim, U. Jo and J. Y. Lee, Expanded multiple-resonance structure for highly efficient narrowband deep-blue organic light-emitting diodes, *Mater. Today*, 2023, **69**, 88–96.
- 7 C. Cao, J.-H. Tan, Z.-L. Zhu, J.-D. Lin, H.-J. Tan, H. Chen, Y. Yuan, M.-K. Tse, W.-C. Chen and C.-S. Lee, Intramolecular Cyclization: A Convenient Strategy to Realize Efficient BT.2020 Blue Multi-Resonance Emitter for Organic Light-Emitting Diodes, *Angew. Chem., Int. Ed.*, 2023, **62**, e202215226.
- 8 T. Hatakeyama, K. Shiren, K. Nakajima, S. Nomura, S. Nakatsuka, K. Kinoshita, J. Ni, Y. Ono and T. Ikuta, Ultrapure Blue Thermally Activated Delayed Fluorescence Molecules: Efficient HOMO-LUMO Separation by the Multiple Resonance Effect, *Adv. Mater.*, 2016, **28**, 2777–2781.
- 9 D. H. Ahn, S. W. Kim, H. Lee, I. J. Ko, D. Karthik, J. Y. Lee and J. H. Kwon, Highly efficient blue thermally activated delayed fluorescence emitters based on symmetrical and rigid oxygen-bridged boron acceptors, *Nat. Photonics*, 2019, **13**, 540–546.
- 10 H. J. Kim and T. Yasuda, Narrowband Emissive Thermally Activated Delayed Fluorescence Materials, *Adv. Opt. Mater.*, 2022, **10**, 2201714.
- 11 X. Wu, B.-K. Su, D.-G. Chen, D. Liu, C.-C. Wu, Z.-X. Huang, T.-C. Lin, C.-H. Wu, M. Zhu, E. Y. Li, W.-Y. Hung, W. Zhu and P.-T. Chou, The role of host-guest interactions in organic emitters employing MR-TADF, *Nat. Photonics*, 2021, **15**, 780–786.
- 12 P. K. Samanta, D. Kim, V. Coropceanu and J.-L. Bredas, Up-Conversion Intersystem Crossing Rates in Organic Emitters for Thermally Activated Delayed Fluorescence: Impact of the Nature of Singlet vs Triplet Excited States, *J. Am. Chem. Soc.*, 2017, **139**, 4042–4051.
- 13 M. K. Etherington, J. Gibson, H. F. Higginbotham, T. J. Penfold and A. P. Monkman, Revealing the spin-vibronic coupling mechanism of thermally activated delayed fluorescence, *Nat. Commun.*, 2016, **7**, 13680.
- 14 X. Fan, X. Hao, F. Huang, J. Yu, K. Wang and X. Zhang, RGB Thermally Activated Delayed Fluorescence Emitters for Organic Light-Emitting Diodes toward Realizing the BT.2020 Standard, *Adv. Sci.*, 2023, **10**, 2303504.
- 15 H. Lim, H. J. Cheon, S.-J. Woo, S.-K. Kwon, Y.-H. Kim and J.-J. Kim, Highly Efficient Deep-Blue OLEDs using a TADF Emitter with a Narrow Emission Spectrum and High Horizontal Emitting Dipole Ratio, *Adv. Mater.*, 2020, **32**, 2004083.
- 16 J. W. Sun, J. Y. Baek, K.-H. Kim, C.-K. Moon, J.-H. Lee, S.-K. Kwon, Y.-H. Kim and J.-J. Kim, Thermally Activated Delayed Fluorescence from Azasiline Based Intramolecular Charge-Transfer Emitter (DTPDDA) and a Highly Efficient Blue Light Emitting Diode, *Chem. Mater.*, 2015, **27**, 6675–6681.
- 17 K. T. Shigehiro Yamaguchi, Silole-containing  $\sigma$ - and  $\pi$ -conjugated compounds, *J. Chem. Soc., Dalton Trans.*, 1998, 3693–3702.
- 18 Y. H. Lee, W. Lee, T. Lee, D. Lee, J. Jung, S. Yoo and M. H. Lee, Blue TADF Emitters Based on B-Heterotriangulene Acceptors for Highly Efficient OLEDs with Reduced Efficiency Roll-Off, *ACS Appl. Mater. Interfaces*, 2021, **13**, 45778–45788.
- 19 C. Li, Y. Luo, Y. Huang, H. Qiu and Z. Lu, A Low-Cost Test Method for Accurate Detection of Different Excited-State Species with a Lifetime Span over 5 Orders of Magnitude in One Time Window, *Anal. Chem.*, 2023, **95**, 8150–8155.
- 20 J. Hwang, H. Kang, J.-E. Jeong, H. Y. Woo, M. J. Cho, S. Park and D. H. Choi, Donor engineered Deep-Blue emitters for



- tuning luminescence mechanism in Solution-Processed OLEDs, *Chem. Eng. J.*, 2021, **416**, 129185.
- 21 S. Jiang, Y. Yu, D. Li, Z. Chen, Y. He, M. Li, G.-X. Yang, W. Qiu, Z. Yang, Y. Gan, J. Lin, Y. Ma and S. J. Su, Sulfone-Embedded Heterocyclic Narrowband Emitters with Strengthened Molecular Rigidity and Suppressed High-Frequency Vibronic Coupling, *Angew. Chem., Int. Ed.*, 2023, **62**, e202218892.
- 22 J. Liu, Y. Zhu, T. Tsuboi, C. Deng, W. Lou, D. Wang, T. Liu and Q. Zhang, Toward a BT.2020 green emitter through a combined multiple resonance effect and multi-lock strategy, *Nat. Commun.*, 2022, **13**, 4876.
- 23 H.-T. Feng, J. Zeng, P.-A. Yin, X.-D. Wang, Q. Peng, Z. Zhao, J. W. Y. Lam and B. Z. Tang, Tuning molecular emission of organic emitters from fluorescence to phosphorescence through push-pull electronic effects, *Nat. Commun.*, 2020, **11**, 2617.
- 24 H. Lee, R. Braveenth, J. D. Park, C. Y. Jeon, H. S. Lee and J. H. Kwon, Manipulating Spectral Width and Emission Wavelength towards Highly Efficient Blue Asymmetric Carbazole Fused Multi-Resonance Emitters, *ACS Appl. Mater. Interfaces*, 2022, **14**, 36927–36935.

